PLOS PATHOGENS

3-Dimensional organization and dynamics of the microsporidian polar tube invasion machinery

Pattana Jaroenlak[1], **Michael Cammer**[2], **Alina Davydov**[1], **Joseph Sall**[2], **Mahrukh Usmani**[1], **Feng-Xia Liang**[2], **Damian C. Ekiert**[1,3]*, **Gira Bhabha**[1]*

1 Skirball Institute of Biomolecular Medicine and Department of Cell Biology, New York University School of Medicine, New York, New York, United States of America, **2** Microscopy Laboratory, Division of Advanced Research Technologies, New York University School of Medicine, New York, New York, United States of America, **3** Department of Microbiology, New York University School of Medicine, New York, New York, United States of America

* damian.ekiert@ekiertlab.org (DCE); gira.bhabha@gmail.com (GB)

Abstract

Microsporidia, a divergent group of single-celled eukaryotic parasites, harness a specialized harpoon-like invasion apparatus called the polar tube (PT) to gain entry into host cells. The PT is tightly coiled within the transmissible extracellular spore, and is about 20 times the length of the spore. Once triggered, the PT is rapidly ejected and is thought to penetrate the host cell, acting as a conduit for the transfer of infectious cargo into the host. The organization of this specialized infection apparatus in the spore, how it is deployed, and how the nucleus and other large cargo are transported through the narrow PT are not well understood. Here we use serial block-face scanning electron microscopy to reveal the 3-dimensional architecture of the PT and its relative spatial orientation to other organelles within the spore. Using high-speed optical microscopy, we also capture and quantify the entire PT germination process of three human-infecting microsporidian species *in vitro*: *Anncaliia algerae*, *Encephalitozoon hellem* and *E. intestinalis*. Our results show that the emerging PT experiences very high accelerating forces to reach velocities exceeding 300 μm·s^{-1}, and that firing kinetics differ markedly between species. Live-cell imaging reveals that the nucleus, which is at least 7 times larger than the diameter of the PT, undergoes extreme deformation to fit through the narrow tube, and moves at speeds comparable to PT extension. Our study sheds new light on the 3-dimensional organization, dynamics, and mechanism of PT extrusion, and shows how infectious cargo moves through the tube to initiate infection.

Author summary

Microsporidia infect a wide range of hosts: from economically important invertebrates such as silkworms and honey bees, to vertebrates including humans, where infection in immunocompromised patients can be fatal. In order to infect the host, microsporidia utilize a unique harpoon-like invasion organelle called the polar tube (PT), which serves as a

---

pathway for transport of infectious cargo to the host. Knowledge of how the long PT is packaged in the spore, the kinetics of its firing and how the cargo is transported through the PT are still poorly understood. We use electron microscopy techniques to generate 3D reconstructions of intact spores, which reveal the configuration of the PT and other organelles within. Using high-speed live-cell imaging, we capture and quantify the kinetics of PT firing, and how cargo is deformed during transport through the narrow PT. Our study provides new insights into architecture and dynamics of the PT, which serve as foundations for our understanding of microsporidia infection.

Introduction

Intracellular pathogens use a diverse array of mechanisms to enter and infect new host cells[1–3]. Microsporidia are a group of single-celled intracellular parasites that have developed one of the most dramatic, yet poorly understood, mechanisms of host cell invasion. Microsporidia are highly diverged from other extant eukaryotes, and are thought to be an early branching sister group to fungi[4,5]. Microsporidia infect a wide range of hosts, including nematodes[6,7], insects[8,9], and vertebrates[10–12]. In humans, microsporidia are commonly found in immunocompromised patients, and lead to opportunistic infections, such as intestinal[13], ocular [14], respiratory[15], and systemic diseases[16]. As obligate intracellular parasites with reduced genomes[17], they are dependent on the host for replication[18,19]. Prior to exiting the host cell, microsporidia form spores, which are the only form of the organism that can survive outside of a host.

To initiate infection of a new cell, these parasites have evolved a unique, harpoon-like invasion apparatus called the polar tube (PT)[19–21] that is present in all microsporidian species. The PT is tightly coiled within the dormant spore, resembling a spring[22,23]. When triggered, the PT transitions within a few hundred milliseconds from a spring-like coil to an extended linear tube, which in some species is more than 100 μm long[24,25]. The extended tube may penetrate or latch onto the target cell membrane to anchor the spore to the host cell [22,23,26,27]. The hollow PT is then poised to serve as a conduit for infectious material (also called sporoplasm) to enter the host cell and establish a replicative niche[28–30]. The entire process, from initiation of PT firing to the completion of cargo transport through the tube, is called spore germination.

While evolutionarily unrelated, the germination of microsporidian spores is conceptually similar to the rapid discharge of nematocysts from cnidarians and dinoflagellates, which is used to hunt prey[31,32]. The process of PT firing has fascinated biologists for more than 100 years[20], yet many fundamental questions remain largely unexplored. While 2D TEM sections have revealed that parts of the PT are coiled in microsporidian spores[21,22,33], the question of how the entire PT is configured within the spore, and its relation to other organelles in 3D is not well understood. The mechanisms that underlie the reconfiguration from a coil to a linear tube during PT extrusion are also a subject of considerable debate; this process has been challenging to study due to the stochastic firing of individual spores and the very fast (millisecond) timescales on which the germination process occurs[24,34]. Finally, the nucleus and other organelles of the microsporidian spore are thought to be translocated through the PT into the host cell. However, the PT is extremely narrow, raising the question: how does the infectious sporoplasm, 2–3 μm in size, move through a tube that is only 100 nm in diameter? Here we use a combination of serial block-face scanning electron microscopy (SBFSEM) and live-cell imaging to reveal the packaging of the long PT inside the much smaller spore, and its

spatial relation to other organelles prior to PT germination. Furthermore, we unveil the dynamics of PT extrusion, and the mechanism of nuclear transport through the PT.

Results

3D reconstruction of *A. algerae* spores

2D transmission electron microscopy (TEM) images of microsporidia have shown that the PT is arranged as a coil within the spore, alongside other organelles[22,33,35,36]. How the coils of the PT are organized in 3D and its spatial relationship to other organelles within the spore is less well understood. We used SBFSEM[37] to generate 3D reconstructions of the PT in intact dormant spores of the microsporidian species *Anncaliia algerae*, which can infect both invertebrate and vertebrate hosts, including humans[38–41]. SBFSEM allows us to automate the sectioning and imaging of a series of 50 nm slices through a block of spores in a high throughput manner[42]. A typical field of view contained approximately 50 spores in several different orientations, from which we reconstructed 20 spores in 3D (Fig 1A, S1 Table).

We segmented the outermost layer of the spore, the exospore, as well as the underlying chitinous endospore, which is adjacent to the plasma membrane (Fig 1B, S1 Video). In the egg-shaped *A. algerae* spores, the exospore layer is uniformly 0.16 ± 0.03 μm thick, and the thickness of the endospore varies from 0.14 μm to less than 0.08 μm towards the anterior tip of the spore. We found that the apical part of the endospore is the thinnest, as previously reported
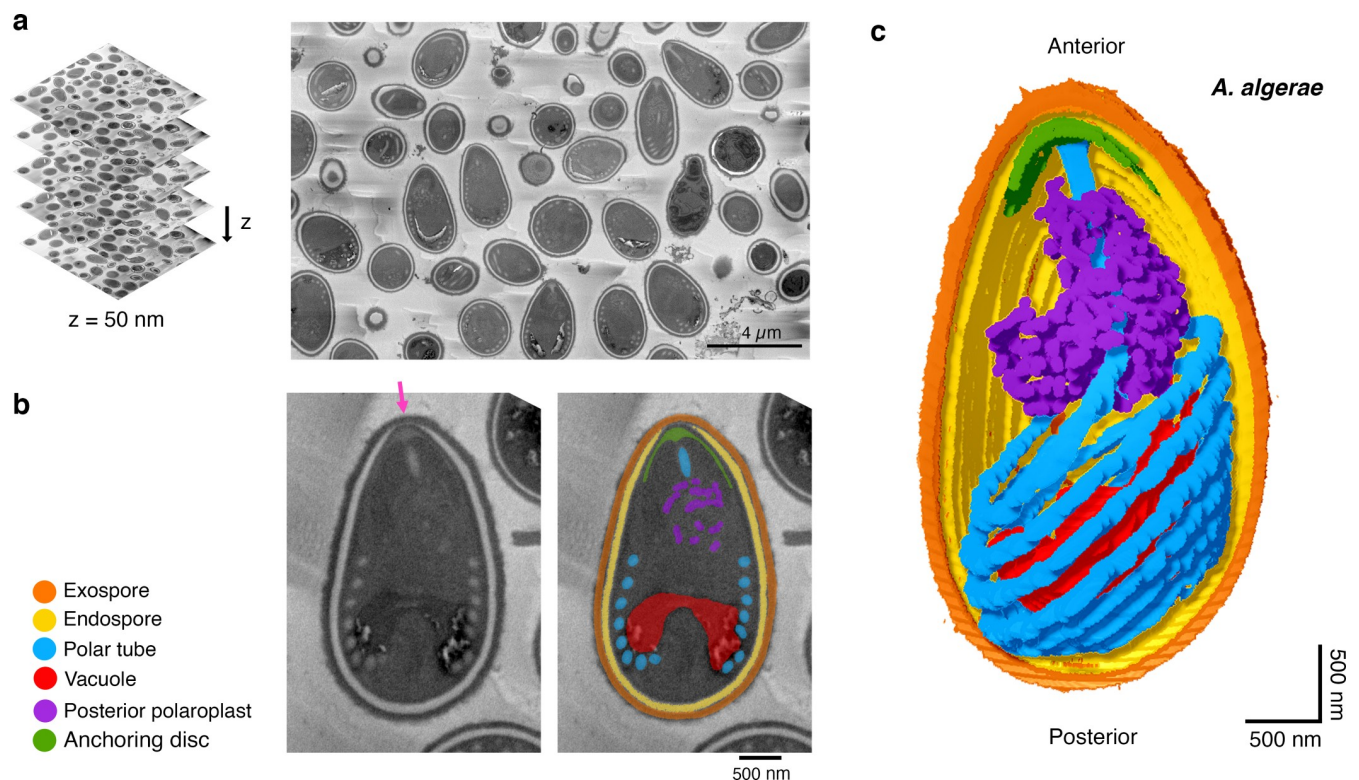
Fig 1. Serial block-face scanning electron microscopy imaging of intact *A. algerae* spores. (a) Representative data from SBFSEM imaging. Samples were serially sliced at 50 nm thickness (left), and a representative slice is shown (right). **(b)** Representative SBFSEM slice highlighting segmented organelles. Original micrograph is shown (left), as well as the same image with color overlays indicating segmented organelles (right): exospore (orange), endospore (yellow), PT (blue), vacuole (red), posterior polaroplast (purple), and anchoring disc (green). The anterior polaroplast is not segmented, as we do not clearly observe it. Magenta arrow indicates the thinnest part of the endospore layer where the anchoring disc is localized. **(c)** Representative 3D reconstruction of an *A. algerae* spore from SBFSEM data. Each color represents an individual organelle; color code as in **(b)**.

https://doi.org/10.1371/journal.ppat.1008738.g001

[35,43], and this region has been hypothesized to be the site of initiation for PT firing[23,44] (Fig 1B and 1C). The spores are 3.9 ± 0.4 μm in length along the anterior-posterior (A-P) axis (S1A Fig), consistent with previous work[40], and the average spore volume is 8.8 ± 1.4 μm^3 (S1B Fig).

Spatial organization of the polar tube in dormant *A. algerae* spores

We segmented the entire *A. algerae* PT to obtain spatial information on how it is organized in the dormant spore (Fig 1C, S1 Video). The PT occupies only ~3.5% of the total spore volume (S1B Fig), yet visually is the most striking feature of the spores when imaged by either SBFSEM or 2D TEM. As previously reported[45], the PT can be divided into two main parts: 1) a linear segment that emanates from the anterior tip of the spore and extends towards the posterior end, and 2) a coil of PT around the middle and posterior end of the spore (Fig 2A). At least two models for the connection between these parts have been proposed (S2 Fig). In the first model, the linear segment extends nearly the length of the spore, and connects to the posterior end of the coiled region[46]. In the second model, the linear segment is shorter, and connects with the anterior end of the coiled region[44]. Our data show that the straight segment connects to the anterior end of the coiled region (Fig 2A), consistent with the second model. The coils of the PT are approximately parallel to each other, but the stack of coils is tilted relative to the A-P axis of the spore (Fig 2B, S1D Fig). Here we found that the coiled segment of the PT consists of 7 turns on average (S1C Fig), in contrast to previous data, which suggested 8–11 coils[40]. The differences may be due to differences in the source of spores or propagation of the spores in different hosts.

Remarkably, in every spore examined the PT takes the form of a right-handed helix (Fig 2C). In the absence of any mechanism to bias PT assembly, the expectation would be a 50:50 mixture of left-handed and right-handed helices. This strong bias towards a right-handed helix implies the presence of an organizing principle. One explanation is that handedness could arise from the physical properties of a polymer, possibly formed by the polar tube proteins (PTPs). Five PTPs have been reported in microsporidia[19,47–49] and three of them (PTP1-3) localize along the entire length of the PT[48], likely acting as key structural elements. The presence of chirality in the PT is consistent with other biopolymers—such as DNA, actin filaments, and microtubules—which adopt superhelical coils with characteristic twist and handedness under strain. Indeed, recent cryo EM images and corresponding Fourier transforms of the PT show clearly repeating patterns along the tube[25]. Alternatively, or in addition, this right-handed bias may arise from asymmetry in the machinery involved in PT assembly.

We observed heterogeneity at the posterior end of the PT among spores, which can be divided into two main classes (Fig 2D). In the majority of spores, the PT terminates abruptly with a clean, blunt posterior end, remaining well-aligned with the preceding coils. However, in a few spores we observed irregular, tangled ends (Fig 2D, S3 Fig). The significance of blunt versus tangled PT ends is unclear, but the tangled ends may, for example, result from different developmental stages of the spores, or from abnormal development of the PT during spore formation[50]. It seems likely that these tangled ends pose a problem for PT extrusion, and if not resolved may result in incomplete germination and failed infection.

Configuration of organelles surrounding the PT in *A. algerae*

In addition to the PT, we segmented other organelles, including the anchoring disc, vacuole, and posterior polaroplast (Fig 1B and 1C, S1 Video). First, the anchoring disc forms an umbrella-shaped structure at the anterior tip of the spore, underlying the thinnest region of the endospore, as previously described[35,51] (Fig 1B and 1C). The anchoring disc is thought
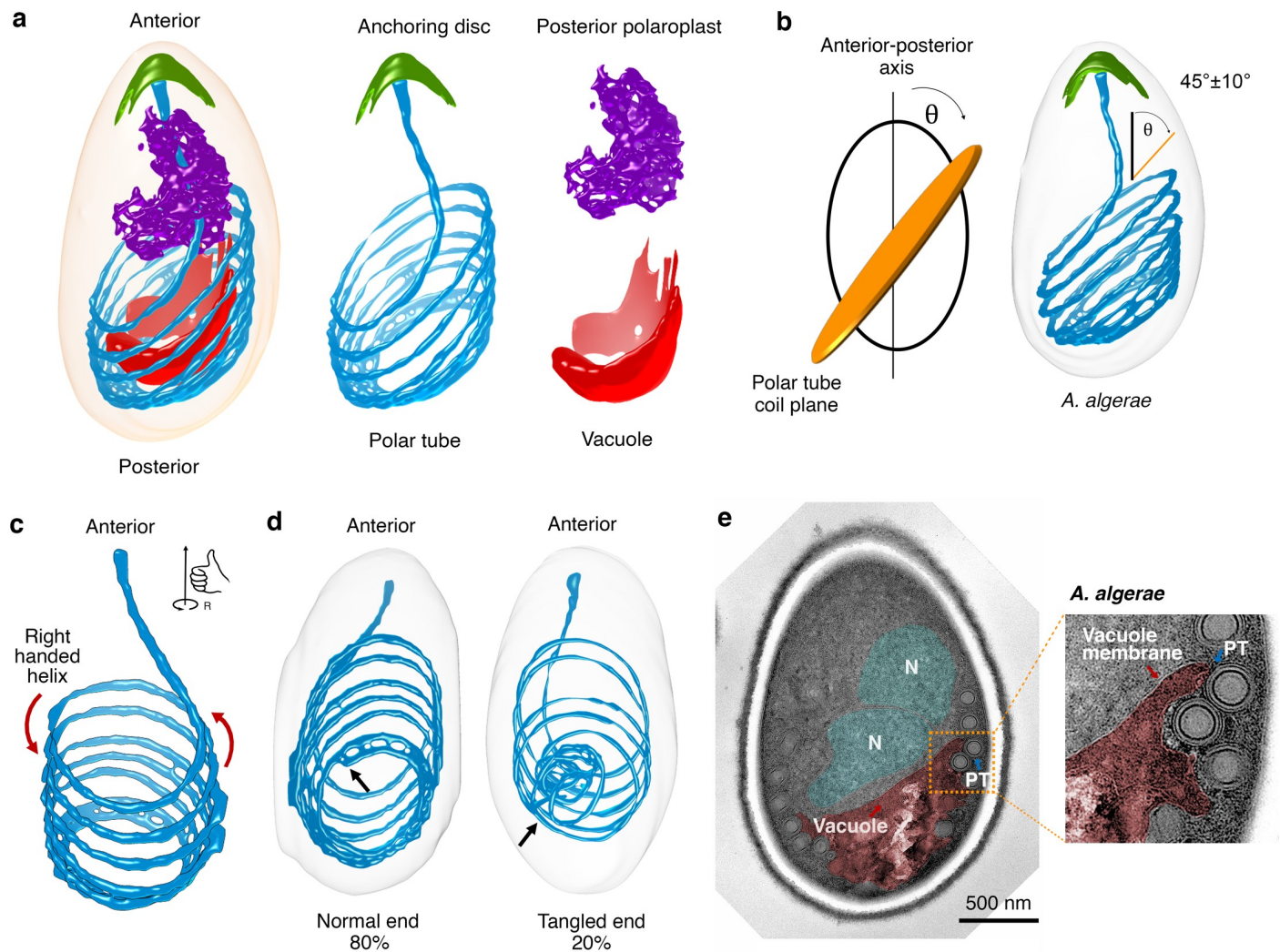
Fig 2. Configuration of the PT and other organelles in intact *A. algerae* spores. (a) Representative 3D reconstruction of an *A. algerae* spore showing the relative orientations of the PT (blue), anchoring disc (green), posterior polaroplast (purple), and vacuole (red). **(b)** Measurement of the angle of PT coils relative to the anterior-posterior (A-P) axis of the spore. Schematic showing how the angle was measured between the A-P axis and the PT coil plane (left). Representative spore with the average angle and standard deviation annotated (right, n = 18). See also S1D Fig. **(c)** Chirality of the *A. algerae* PT. Red arrows indicate the right-handed helix of the PT. **(d)** Heterogeneity of PT ends observed in *A. algerae* PTs (n = 20). Black arrows indicate the location of the PT end. **(e)** Transmission electron microscopy (TEM) section of an *A. algerae* spore showing interdigitation between vacuole membrane (red) and the PT, and position of the nuclei (N, cyan) relative to the vacuole. Inset shows the region boxed in orange.

to be the site of spore germination, and thus some rearrangement or disruption of the anchoring disc is required to allow egress of the PT. Second, the vacuole at the posterior end of the spore occupies approximately 6.9% of the spore volume, and is roughly bowl-shaped (Fig 2A, S1B Fig). The vacuole has previously been shown to expand during the germination process, and one possibility is that it plays an active role in facilitating PT extension and the translocation of spore contents through the PT[34,52]. Our 2D TEM sections show that the vacuole is surrounded by a single membrane (Fig 2E). The convex side is in close proximity to the posterior pole, and the concave side faces towards the anterior end of the spore (Fig 2A and 2E). While there is no clear cellular structure interacting with the concave surface of the vacuole in our SBFSEM images, examination of 2D TEM images reveals that the nucleus often rests against this depression in the vacuole (Fig 2E). Interestingly, the vacuolar membrane is tightly

interdigitated between PT coils (Fig 2E, S4A Fig). Third, the polaroplast is a multi-layered membranous organelle that is thought to be important during the germination process, perhaps providing membrane to accommodate the increased cell surface area during cargo transport through the PT[52]. Typically, the polaroplast consists of two regions with different morphologies, as observed by 2D TEM[30,33]: anterior polaroplast and posterior polaroplast (S4 Fig). Reconstruction of the posterior polaroplast showed that it snugly surrounds the linear part of the PT (Fig 2A), possibly stabilizing this region and is well-positioned to contribute membrane to the extending tube as it exits the spore.

Comparison of *E. hellem* and *A. algerae* 3D reconstructions

To assess whether the PT configuration and the relative orientation of other organelles are conserved in other microsporidian species, we carried out SBFSEM analysis of another human-infecting microsporidian species, *Encephalitozoon hellem* (Fig 3A, S1 Table). We segmented the spore wall layers, PT, anchoring disc, and anterior polaroplast (Fig 3B, S2 Video). While the overall organization of organelles in *E. hellem* spores is similar to the organization in *A. algerae* spores, including a right-handed helical arrangement of the PT (Fig 3C), there are also some notable differences. First, in contrast to the egg-shaped *A. algerae* spores, the *E. hellem* spores are more cylindrical (Fig 3C). The length of the *E. hellem* spores is 2.8 ± 0.3 μm along the A-P axis, and the volume is approximately half that of *A. algerae* (S1A and S1B Fig). Second, the spacing between PT coils is smaller in *E. hellem* (an average distance of 0.12 ± 0.03 μm, compared with 0.22 ± 0.02 μm for *A. algerae* (Fig 3D)), resulting in a more tightly packed coil. Third, in most *E. hellem* spores, the anchoring disc is located off-center with respect to the apical tip of the spore, rather than at the center of the apical tip as in *A. algerae* (Fig 3E). The region surrounding the anchoring disc is the thinnest part of the spore wall (Figs 1B and 3B), regardless of whether it is at the apical tip, or off-centered, and this region is where the PT is expected to exit the spore. Overall, the SBFSEM results provide insights into how the PT is packed inside the spore, and these data provide a static snapshot of the PT in its pre-germination state.

Kinetics of polar tube germination

In order to infect the host, microsporidia must first extend the PT to penetrate a target cell. This process occurs extremely rapidly[24,25,34], making it challenging to image in real time. To better understand the kinetics and mechanics of PT germination, we performed high-speed, live-cell imaging to capture *in vitro* PT germination events in three microsporidian species that infect humans: *A. algerae*, *E. hellem*, and *Encephalitozoon intestinalis*. Although the *in vivo* triggers for PT firing are not well understood, *in vitro* triggers have been reported[53–56]. We used small variations of these conditions to optimize PT firing *in vitro* for our light microscopy assay (see Methods), and captured the entire germination process, including release of the cargo after transport through the PT (Fig 4A, S3–S5 Videos, S2 Table). In all three species, we observed three distinct phases of the germination process: 1) PT elongation, 2) a static phase, where the PT length does not change, and 3) emergence of cargo at the distal end of the PT. PT elongation occurs rapidly (Fig 4B, S5–S7 Figs); the time to reach 90% PT extension (T_{EXT90}) is significantly shorter in *E. intestinalis* (T_{EXT90} 160 ± 20 ms; Fig 4C) and *E. hellem* (T_{EXT90} 290 ± 200 ms) compared with *A. algerae* (T_{EXT90} 830 ± 170 ms). The entire germination process, from the start of PT extrusion to cargo ejection, is completed in less than 500 ms in *E. hellem* and *E. intestinalis*, and in approximately 1.6 seconds in *A. algerae*. We observed that the PT emerges from the center of the apical tip in *A. algerae* and off-center in *E. hellem* and *E. intestinalis* (S8 Fig). This is consistent with the preferential positioning of the anchoring
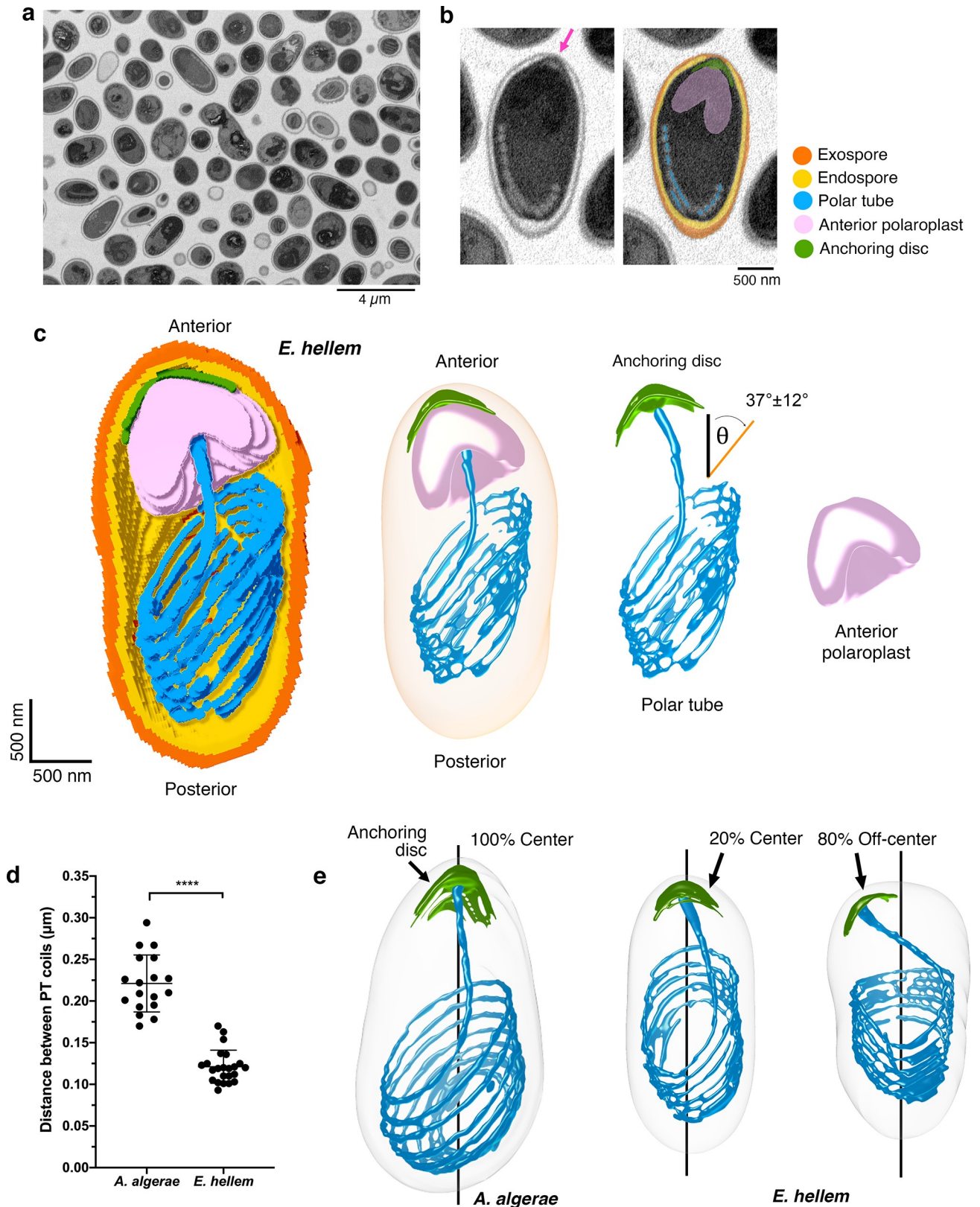
Fig 3. Serial block-face scanning electron microscopy imaging of *E. hellem* spores and comparison with *A. algerae*. (a) A representative slice from SBFSEM imaging of *E. hellem* spores. (b) Representative SBFSEM slice highlighting segmented organelles. Original micrograph is shown (left), as well as

the same image with color overlays indicating segmented organelles (right): exosore (orange), endospore (yellow), PT (blue), anterior polaroplast (pink), and anchoring disc (green). Magenta arrow indicates the thinnest part of the endospore layer where the anchoring disc is localized. **(c)** Representative 3D reconstruction of an *E. hellem* spore from SBFSEM data. Each color represents an individual organelle; color code as in (b). We did not observe any tangled PT ends in *E. hellem* spores. The average angle of *E. hellem* PT coils relative to the A-P axis is annotated with a standard deviation (n = 20, See also S1D Fig). The angle measurement was performed as in Fig 2B. **(d)** Quantification of the distance between the PT coils in *A. algerae* and *E. hellem*. Error bars represent standard deviation (n = 18 for *A. algerae* and n = 20 for *E. hellem*), ****p<0.0001 (unpaired Student's t-test). **(e)** Position of the anchoring disc (AD, green) relative to the spore coat. Black line indicates the anterior-posterior (A-P) axis of the spore. Coincidence of the AD and the A-P axis was scored as "center", indicating that the AD is at the apical tip of the spore. Separation of the AD from the A-P axis was scored as "off-center", indicating that the AD is not centered at the apical tip of the spore (n = 18 for *A. algerae* and n = 20 for *E. hellem*).

disc in our SBFSEM data, at the center of the apical tip in *A. algerae* and off-center in *E. hellem* spores, supporting the idea that the anchoring disc position determines the PT exit site (Fig 3E).

In phase 1, the PT is fired and elongates to its maximum length (Fig 4A, S5–S7 Figs). Our data show that on average, the maximum velocity (V_{max}) of PT firing is 235 ± 61 μm·s^{-1} and the maximum acceleration (A_{max}) is $1,503 \pm 1,082$ μm·s^{-2} in *A. algerae* (Fig 4D and 4E). The V_{max} we observe is approximately double the previously reported value for this species[24], which may reflect differences in *A. algerae* spores purified from different sources or more accurate measurements due to higher temporal resolution. In *E. hellem* and *E. intestinalis*, V_{max} and A_{max} are higher than that measured for *A. algerae*. The V_{max} and A_{max} reaches 336 ± 142 μm·s^{-1} and $5,219 \pm 2,521$ μm·s^{-2} for *E. hellem*, and 290 ± 38 μm·s^{-1} and $5,045 \pm 2,242$ μm·s^{-2} for *E. intestinalis*, respectively (Fig 4D and 4E). In contrast, other cellular processes involving movement are typically slower, such as organelle transport in cells by motor proteins (~0.51 μm·s^{-1} for human kinesin[57], ~1 μm·s^{-1} for porcine dynein[58]), gliding motility of apicomplexan parasites (1–3 μm·s^{-1})[59], and mobility of zoospores from chytrid fungi (~104 μm·s^{-1})[60].

In phase 2, the PT is fully extended and remains static at its maximum length: on average, 101, 53 and 36 μm for *A. algerae*, *E. hellem*, and *E. intestinalis* respectively (S9A Fig). In *A. algerae* this phase persists for 790 ± 360 ms (S9C Fig), and we hypothesize that during this time, the infectious cargo is traveling through the PT. If cargo transport begins once the tube is fully extended and all the species transport cargo at the same rate, we would expect phase 2 in *E. hellem* and *E. intestinalis* to be approximately 400 ms, since their PTs are approximately half the length of the *A. algerae* PT. However, we observe *E. hellem* and *E. intestinalis* spend less time in this phase than predicted (60–140 ms; S9C Fig), suggesting that either cargo transport is faster in these species, or that cargo may begin moving through the PT before extension is completed. Intriguingly, for *E. hellem*, in which the source of the spores was the same for SBFSEM experiments and light microscopy (LM) experiments, we found that the fully extended PTs observed by LM are more than twice the length of pre-germination PTs packaged inside the spore, as assessed by SBFSEM (Fig 4H, S9D Fig, see Methods). A previous study has also suggested that the PT length outside the spore may be longer than when it is packed inside the spore[22]. The PT is thought to be built of repetitive protein polymers[25], and our observation raises the possibility that a significant conformational change may occur in some or all of these proteins between pre-germination and post-germination states, potentially leading to a change in PT length.

In phase 3, the cargo is expelled at the distal end of the PT, and appears approximately circular in shape (Fig 4A). The cargo remains attached to the tube for the duration of the experiment, and it is unclear what mediates this contact. There may be specific interactions between components of the PT and the cargo, or alternatively, some cargo may remain inside the tube itself, thereby creating a membranous bridge that leads to stable adhesion. When we continued imaging for several seconds after the cargo had been expelled, we observed that the *E. hellem*
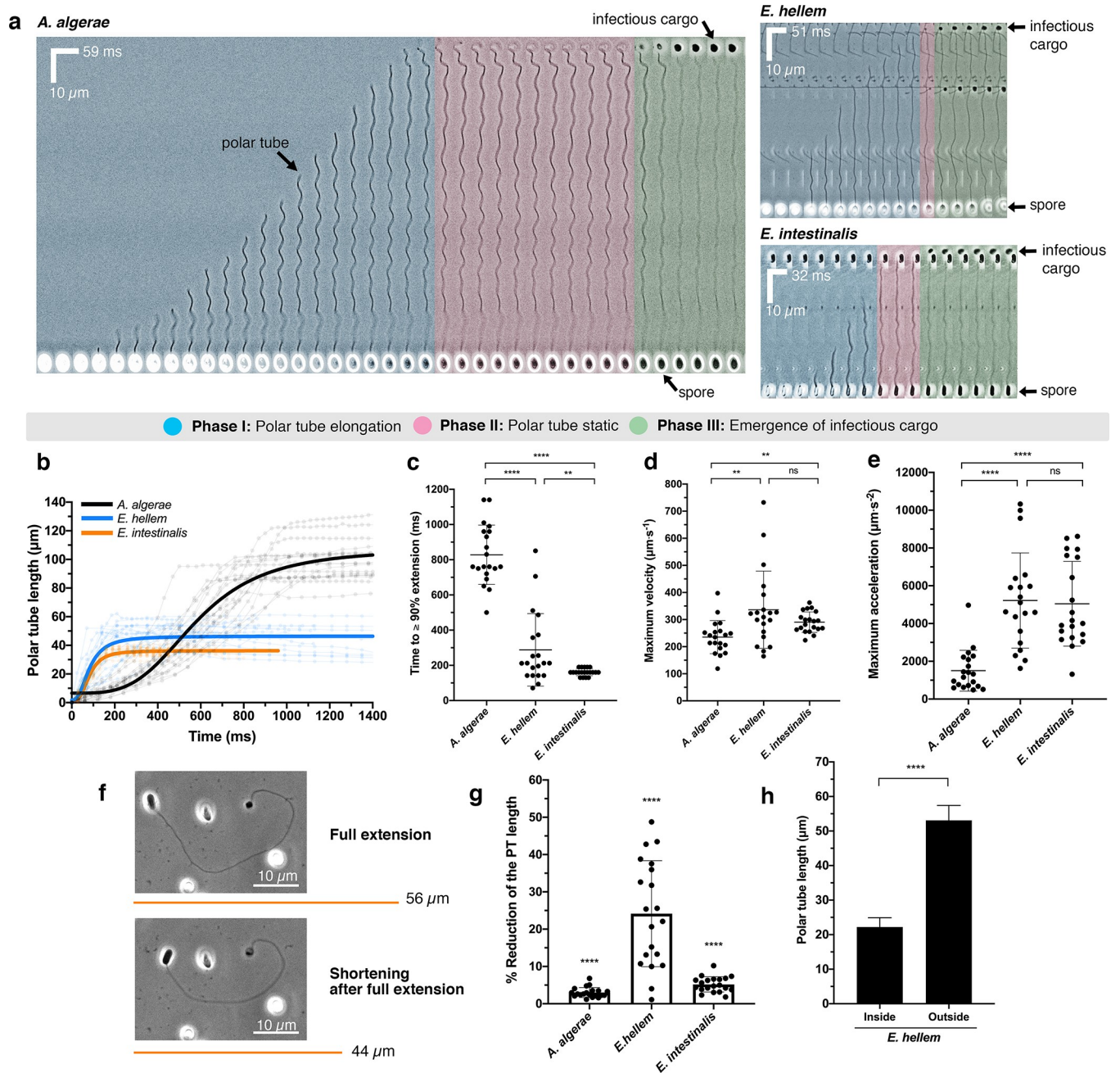
Fig 4. Live-cell imaging of PT germination. (a) Kymographs showing representative spore germination events from three microsporidian species: *A. algerae*, *E. hellem*, and *E. intestinalis*. Scale bars for distance and time intervals are shown on each kymograph. Three phases of the germination process are color-coded. The *A. algerae* PT appears to have a wavy pattern as it emerges from the spore, possibly forming a spiral, while the *E. hellem* and *E. intestinalis* PTs are less wavy in nature. As infectious cargo emerges from the distal end of the PT, the amplitude of the waveform is reduced, as has been previously noted[24]. After the *A. algerae* PT is fully extended, the distal end of the fired PT is curved and forms a hook-like structure, as previously described[25]. See also S3–S5 Videos. **(b)** Quantification of the PT length as a function of time for *A. algerae* (black), *E. hellem* (blue), and *E. intestinalis* (orange) (n = 20 for each species). The raw data are shown as faint lines with time points indicated as circles. The overall trends of each species were fitted (see Methods) and are represented as thick lines in the corresponding color. **(c)** Time taken for PT to extend to $\geq 90\%$ (T_{EXT90}) of its maximum length (n = 20 for each species). ****$p<0.0001$, **$p = 0.0096$ (unpaired Student's t-test). **(d)** Average maximum velocity of PT extension calculated as described in Methods (n = 20 for each species). **$p = 0.006$; ns, not significant (unpaired Student's t-test). **(e)** Average maximum acceleration of PT extension (n = 20 for each species). ****$p<0.0001$; ns, not significant (unpaired Student's t-test). **(f)** Shortening of the *E. hellem* PT after the full extension (maximum length) has been reached and cargo ejected. Representative phase-contrast micrographs are shown, and orange lines represent the length of the PT quantified from the micrographs. **(g)** Reduction of PT length measured 3 seconds after sporoplasm ejection, as a percentage of the maximum PT length (n = 20 for each species, see other representations of these data in S9A and S9B Fig). The PT shortens by 3%, 24%, and 5% for *A. algerae*, *E. hellem*, and *E. intestinalis*, respectively. ****$p<0.0001$ (One sample t-test). **(h)** Comparison of the

PT length for *E. hellem*, in dormant spores, obtained from SBFSEM (labeled "inside") and the maximum PT length after germination, obtained from live-cell optical microscopy experiments (labeled "outside") (n = 20, see Methods for how these measurements were made). ****p<0.0001 (unpaired Student's t-test). All error bars in this figure represent standard deviations.

PT rapidly shortens (Fig 4F), and a similar observation has been reported for *A. algerae*[24]. To assess this observation quantitatively, we measured the length of the PT after germination is complete (full PT extension), and also 3 s later. The PT of *E. hellem* shortens by 24%, while the *A. algerae* and *E. intestinalis* PTs shorten by only 3% and 5% respectively (Fig 4G, S9A and S9B Fig, S6 Video). This suggests that there are differences in the mechanics, plasticity and behavior of the PT even between closely related species such as *E. hellem* and *E. intestinalis*. Shortening of the *E. hellem* PT appears to be distributed across the length of the tube, as opposed to shortening due to retraction of the tube back inside the spore coat (S6 Video).

Occasionally, we observed incomplete germination of the PT in all three species, which we define as being stuck in phase 1 or phase 2: the PT may not be fully extended, or it is extended but no cargo is observed at the distal end of the tube (S10A and S10B Fig, S7–S9 videos). In these events, the time to maximum extension of the PT was longer than in productive germination events (S10C Fig). Incomplete PT firing events have been previously described[24], and may represent spores that are not infectious, since cargo does not emerge at the distal end of the tube.

Cargo transport through the tube

An enigma of the microsporidian invasion process is that the cargo to be transported through the tube is much larger than the diameter of the tube itself. While it is unclear precisely what is transferred from the spore to the host cell, at the very least the nucleus containing the parasite genome must be transported through the tube[33,61]. In the case of *A. algerae*, there are two nuclei[23], and the diameter of each nucleus is about 0.7 μm, while the diameter of the PT is approximately 100 nm, as measured from negative stain images of the PT[25]. The nucleus is at least 7 times larger in diameter than the PT, and this mismatch in scale must be overcome to achieve cargo transport through the tube. As tools for genetic modification and transgenesis are not yet available for microsporidia, labeling specific subcellular structures for live-cell imaging is challenging, and consequently tracking the movement of cargo through the polar tube has not been reported.

To track nuclear movement within the spore body during germination, we used NucBlue to stain the nucleus of intact spores, which yields sufficient signal for live-cell imaging (Fig 5A). We used a modified version of our live-cell imaging assay, in which we pre-incubated dormant *A. algerae* spores with NucBlue, and tracked the nucleus during PT firing. We used dual detection of fluorescence and transmission to track the nucleus and to visualize the PT, respectively. Prior to nuclear exit from the spore, we clearly observed two distinct fluorescent lobes, corresponding to the two nuclei in *A. algerae* (Fig 5C, S10 Video). The two nuclei briefly move around and rearrange inside the spore, perhaps in response to the rapid ejection of the PT, then enter the PT together, on a very fast timescale. Interestingly, while T_{EXT90} is 830 ms in *A. algerae* on average, nuclear translocation into the PT begins only ~500 ms after the initiation of PT firing, suggesting that the tube is not fully extended prior to cargo transport (Fig 5C, S11A Fig).

Next, we shifted our attention to monitoring the nucleus as it moves through the PT. Given the discrepancy in diameter between the nucleus and the PT, we hypothesized that either 1) the PT is flexible enough that it could deform to accommodate the nuclei, or 2) the nuclei must deform to fit the PT diameter (Fig 5B). To assess which hypothesis may be correct, we
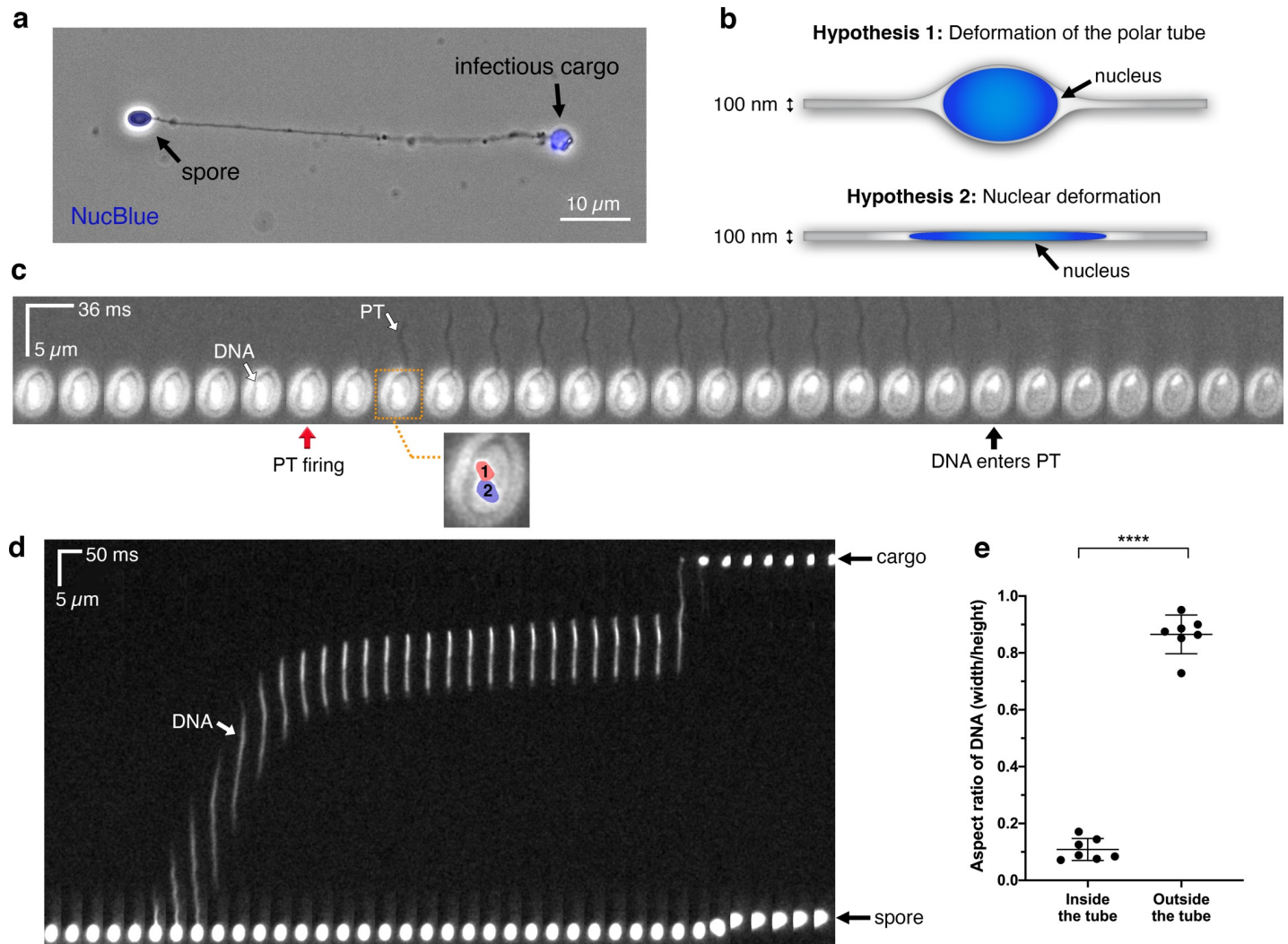
Fig 5. Live-cell imaging of nuclear transport through the PT. (a) Image of a fixed germinated *A. algerae* spore stained with a nuclear dye, NucBlue, overlaid with a phase-contrast image of the same spore. **(b)** Schematic diagrams show two possible hypotheses of how large nuclei may travel through the narrow PT. Nucleus is depicted in blue; in "hypothesis 1" it is drawn as an oval, to scale with the PT (nucleus diameter = ~0.7 μm; PT diameter = ~100 nm). **(c)** Time-lapse images of the two *A. algerae* nuclei inside the spore during PT germination, with a time interval of 36 ms. Nuclei are pre-stained with NucBlue, and white light was applied in order to observe the PT firing event simultaneously. Red arrow indicates the frame in which PT firing is initiated; black arrow indicates the frame in which the nuclei begin to leave the spore body. Inset highlights the two nuclei, labeled with numbers and color overlays, from the frame boxed in orange. **(d)** Kymograph of nuclear translocation through the PT, with a time interval of 50 ms. **(e)** Quantification of the aspect ratio of the nuclei during transport (inside the tube) and after being expelled (outside the tube), which represents the extent of nuclear deformation during the process. Error bars represent standard deviation (n = 7), ****p<0.0001 (paired Student's t-test).

performed live-cell imaging of *A. algerae* PT germination *in vitro*, and monitored the nuclei as they traversed through the PT. Our results show gross deformation of the nuclei on a millisecond timescale as they travel through the PT (Fig 5D, S11B Fig, S11 Video). However, after exiting the tube, the nuclei return to a globular shape (Fig 5D). To better quantify this nuclear deformation, we calculated the aspect ratio (the shortest dimension divided by the longest dimension) of the nuclei inside the PT and after exit from the PT (Fig 5E). The aspect ratio should be close to 1 for an isotropic object (e.g. circle), whereas an aspect ratio less than 1 indicates an elongated object (ellipse). The average aspect ratio of the paired nuclei is 0.11 ± 0.04 inside the tube and 0.87 ± 0.07 after they are expelled, outside the PT (Fig 5E). The nuclei travel through the tube at remarkable velocities, approaching 270 ± 115 μm·s^{-1} (S11D Fig), which is

comparable to PT firing velocities in *A. algerae*. Of note, the nuclei pause within the PT during translocation in all seven movies we recorded *in vitro* (Fig 5D, S11B and S11C Fig, S11 Video). This may reflect a change in the forces that are driving cargo transport through the PT, though it remains to be determined whether pausing also occurs during germination *in vivo*.

Discussion

Mechanistic insights into polar tube germination

Microsporidia comprise an entire phylum of extremely successful parasites, all of which share the common feature of the polar tube infection apparatus. Our data combine spatial and temporal information to provide new insights about how the PT is packed in dormant spores, the PT germination process, and synchronization of PT firing and cargo transport. Synthesizing these data, we present a model for PT germination (Fig 6), in which we can clearly define some aspects of the germination process, while others still remain ambiguous. We focus on *A. algerae*, as we have the most information for this species. In the dormant spore, the PT is a right-handed helix packed at an angle relative to the A-P axis of the spore, and interacts closely with the vacuole. The two nuclei in *A. algerae* are nestled in the bowl-shaped vacuole, and surrounded by the coiled PT (Fig 6A). Previous data suggest that initiation of germination is dependent on osmotic pressure buildup within the spore[62], which may trigger the rupture of the spore wall and PT firing[63]. Once triggered, the PT fires and reaches its full length in under 1 second (T_{EXT90} = ~830 ms). By tracking the nuclei during this germination process, we find that as the germination process initiates, the two nuclei begin to rearrange in the spore (Fig 6B, step 3). Approximately 500 ms after PT firing is initiated, the nuclei exit the spore body together, and deform drastically to fit into the PT. The average time to 50% extension (T_{EXT50}) in *A. algerae* is approximately 600 ms, suggesting that once the tube has reached ~50% extension, cargo transport is initiated. This observation is consistent with a model in which the PT everts[21,64], which would only allow cargo to enter the tube after 50% extension. The velocity at which the cargo is transported through the tube is comparable to the velocity of PT extension, and the cargo regains a globular shape after exiting the PT. Many open questions remain and further studies will be required to definitively address the mechanistic basis of PT germination.

Rapid nuclear deformation in microsporidia

In our study, we observed incredibly fast and large deformation of the nuclei as they traveled through the PT. This is reminiscent of other cell translocation and migration processes, such as immune cells squeezing through tight junctions to exit the bloodstream, or tumor cells penetrating tissues[65–67]. Nuclear deformation is necessary to facilitate tumor cell invasion, as the cells must adapt their shape to accommodate available space within the three-dimensional architecture of the tissue. Two key differences between the nuclear deformation we observe in microsporidia and analogous processes in tumor cell invasion is that the timescale is much faster in microsporidian nuclear transport (milliseconds compared with minutes/hours), and the microsporidian nuclear distortion is much more severe, as assessed by the aspect ratio. During tumor cell invasion and nuclear deformation, DNA damage is reported to occur [68,69]. Given the extent of microsporidian nuclear deformation during transport, it is plausible that the microsporidian genome may also be subject to shearing and other stresses. In migrating cancer cells, nuclear envelope breakdown has also been noted[68,69], which likely enhances deformability of the packaged DNA. Some cancer cells express lower levels of lamins [70–73], which are known to be important cytoskeletal proteins that rigidify the nuclear envelope. While cells expressing low levels of lamin A show a high migration rate through tissues
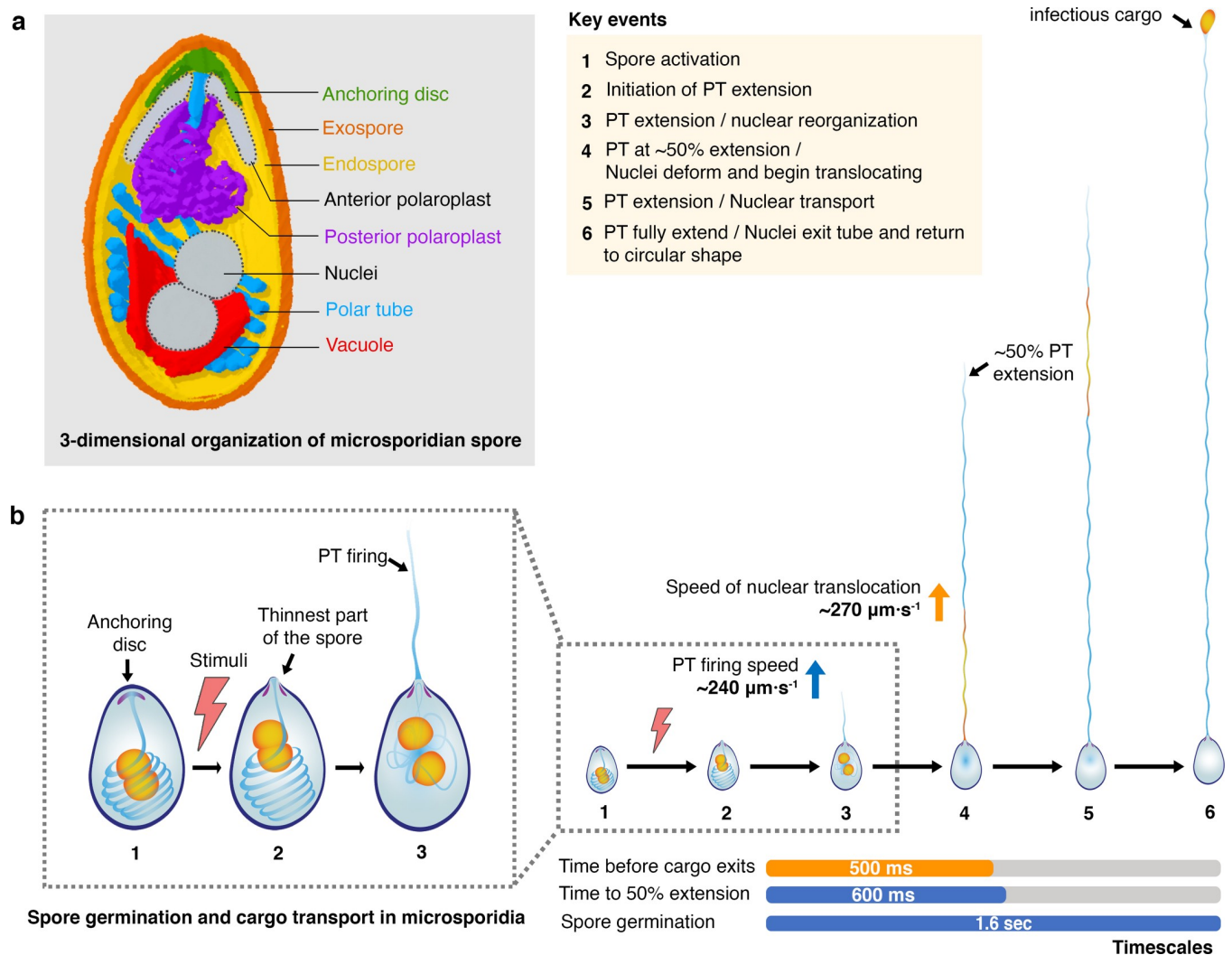
Fig 6. Model for PT germination and nuclear transport through the PT. (a) Model for 3-dimensional organization of a microsporidian spore. Combining our SBFSEM and 2D TEM data for both *A. algerae* and *E. hellem*, we generate a composite 3D model that shows spatial organization of organelles inside the microsporidian spore. Elements that were not observed in the *A. algerae* SBFSEM data (anterior polaroplast and nuclei) have been added manually and are in gray. The anterior part of the PT (blue) is straight and connected to the anchoring disc (green). This part of the PT is surrounded by the anterior (gray) and posterior (purple) polaroplast. The posterior part of the PT is coiled and packed at an angle relative to the A-P axis. The PT resembles a rib cage around the vacuole (red) and nuclei (gray). The vacuole is bowl shaped, and localized beneath the nuclei. **(b)** Model for PT germination and cargo transport in *A. algerae*. (1) The spore is triggered in the presence of a stimulus (*in vivo* triggers remain largely unknown; *in vitro* triggers are described in Methods). (2) PT firing is initiated at the thinnest part of the spore coat, where the anchoring disc is localized. (3) After initiation of PT firing and during Phase I (PT elongation), the nuclei, and presumably other organelles, are reoriented. (4) At the stage in which the PT is extended to just past 50%, the nuclei deform to fit into the PT and exit the spore. (5) Nuclei (and likely other cargo) are translocated through the PT, at a speed comparable to that of PT extension. (6) The nuclei exit the PT and regain a circular shape at the tip of the PT.

[74], overexpression of lamin A has been shown to result in reduced nuclear deformability and impaired cell passage through narrow constrictions[75], consistent with the idea that the presence of lamins contributes substantially to rigidity of the nucleus. In agreement with previous reports that lamins are only present in Metazoans[76,77], we were unable to identify any lamins or homologs in fully sequenced microsporidian genomes[17,78,79]. This suggests that microsporidia may lack lamins entirely, perhaps explaining why nuclear deformation occurs to a much higher degree than in mammalian cells, and on a rapid timescale. Future studies will reveal the nature of cargo transport and address questions of the chromatin state during

nuclear transport, whether the nuclear envelope is intact, and how cargo is modulated once delivered to the host.

Materials and methods

Propagation of microsporidian parasites

A. algerae was propagated either in *Helicoverpa zea* larvae or in Vero cells. *E. hellem* and *E. intestinalis* were propagated in Vero cells. *A. algerae* spores propagated in *H. zea* were purified using a continuous Ludox gradient, as previously described[80], and kindly provided by James J. Becnel and Neil Sanscrainte. To propagate the parasites in Vero cells, microsporidia *A. algerae* (ATCC PRA-168), *E. hellem* (ATCC 50504), and *E. intestinalis* (ATCC 50506) were grown in Vero cells (ATCC CCL-81) using Eagle's Minimum Essential Medium (EMEM) (ATCC 30–2003) with 10% heat-inactivated fetal bovine serum (FBS) at 37˚C and with 5% CO_2. At 70%-80% confluence, parasites were added into a 25 cm^2 tissue culture flask and the media was switched to EMEM supplemented with 3% FBS. Cells were allowed to grow for fourteen days and medium was changed every two days. To purify spores, the infected cells were detached from tissue culture flasks using a cell scraper and placed into a 15 ml conical tube, followed by centrifugation at 1,300 g for 10 min at 25˚C. Cells were resuspended in sterile distilled water and mechanically disrupted using a G-27 needle. The released spores were purified using a Percoll gradient[79]. Equal volumes (5 mL) of spore suspension and 100% Percoll were added to a 15 mL conical tube, vortexed and then centrifuged at 1,800 g for 30 min at room temperature. The purified spore pellets were washed three times with sterile distilled water and stored at 4˚C in distilled water for further analyses.

Germination conditions for microsporidian spores

Germination conditions, to activate PT firing, are different among microsporidian species [53,54,81]. For *A. algerae*, the germination buffer was slightly modified from the previously reported condition[53]. Spore germination was triggered by incubating spores at 30˚C for 30 min in 10 mM Glycine-NaOH buffer pH 9.0 and 100 mM KCl. These conditions typically yield ~70% germination. For both *Encephalitozoon* species, spores were incubated at 37˚C and spore germination was triggered using germination buffer containing 140 mM NaCl, 5 mM KCl, 1 mM $CaCl_2$, 1 mM $MgCl_2$, and 5% (v/v) H_2O_2 at pH 9.5, as previously described[54]. Germination buffer for *Encephalitozoon* species was freshly prepared for each experiment.

Electron microscopy

Purified spores from tissue culture were fixed in 0.1 M sodium cacodylate buffer (pH 7.2) containing 2.5% glutaraldehyde and 2% paraformaldehyde. For transmission electron microscopy, fixed spores were post-fixed with 2% osmium tetroxide (OsO_4), embedded in 2% agar, block stained in 1% aqueous uranyl acetate, and dehydrated using a gradient of cold ethanol. The samples were then transferred in propylene oxide and embedded in EMbed 812 (Electron Microscopy Sciences, catalog #14121). 70 nm thin sections were cut, mounted on copper grids and stained with uranyl acetate and lead citrate. Stained grids were inspected using a Thermo Fisher Talos 120C electron microscope and imaged with a Gatan OneView camera using a nominal magnification of 22,000x corresponding to a pixel size of 0.652 nm/pixel on the specimen.

For serial block-face scanning electron microscopy (SBFSEM), the sample block was mounted on an aluminum 3View pin and electrically grounded using silver conductive epoxy (Ted Pella, catalog #16014). The entire surface of the specimen was then sputter coated with a

thin layer of gold/palladium and imaged using the Gatan OnPoint BSE detector in a Zeiss Gemini 300 VP FESEM equipped with a Gatan 3View automatic microtome. The system was set to cut 50 nm slices, imaged with gas injection setting at 40% (2.9 x 10^{-3} mBar) with Focus Charge Compensation to reduce electron accumulation charging artifacts. Images were recorded after each round of sectioning from the blockface using the SEM beam at 1.5 keV with a beam aperture size of 30 μm and a dwell time of 1.0 μs/pixel. Each frame is 22 x 22 μm with a pixel size of 2.2 nm. Data acquisition occurred automatically using Gatan Digital Micrograph (version 3.31) software. A stack of 150 slices was aligned and assembled using Fiji[82]. A total volume of 22 x 22 x 11 $μm^3$ was obtained from the sample block.

Segmentation of organelles of interest, 3D reconstruction, and quantification of the spore size, volumes and PT length in the intact spores were performed using Dragonfly 4.1 software (Object Research Systems, ORS). SBFSEM sections were automatically aligned using SSD (sum of squared differences) method prior to segmentation. Graphic representation of the spores and PT were performed with either Dragonfly software or UCSF Chimera[83].

Measurement of the PT angles and the distance between coils were made in UCSF Chimera [83]. To facilitate this, two atoms were placed as markers on the anterior-posterior ends of the spore to create an A-P axis. 3 more atoms were placed along the PT coil to generate a plane corresponding to the PT. Then, the PT angles were measured between the A-P axis and the PT plane. To measure the distance between the coils, atoms were manually placed at the center of two adjacent coils, and the distance between these was measured.

Optical microscopy

Live-cell imaging of PT firing. 2 μl of purified *A. algerae* spores obtained from *H. zea* ($6x10^7$ spores/ml) or purified *E. hellem* and *E. intestinalis* spores from tissue culture (~10^8 spores/ml) were mixed with 10 μl of germination buffer. The reaction was placed on ice to prevent PT firing prior to imaging. 2 μl was placed on a poly-L-lysine-coated glass slide (Fisher Scientific, catalog #12-545-78) and sealed with a #1.5 18 x 18 mm coverslip (Fisher Scientific, catalog #12-519-21A). Polar tube firing typically occurred ~2–5 minutes after mixing the spores with the germination buffer. PT firing was imaged using a Nikon Eclipse Ti microscope with a Nikon 60x N.A. 1.4 oil immersion Plan Apochromat Ph3 phase-contrast objective lens. An Andor Zyla 5.5 megapixel sCMOS camera was used, which provided a wide field of view at 14–50 frames per second with 3–35 ms exposure time, no binning was applied. The microscope was equipped with an environmental chamber which was set at 30˚C for *A. algerae*[24] and 37˚C for *Encephalitozoon* species[54].

Fixed cell imaging. 4 μl of *A. algerae* spores purified from infected *H. zea* (10^8 spores/ml) was incubated with 20 μl of germination buffer at 30˚C for 30 min. 40 μl of NucBlue Live ReadyProbes Reagent (Invitrogen, catalog #R37605) was added and the reaction was incubated at 25˚C for 20 min. Spores were pelleted by centrifugation at 1,000 g for 1 min at room temperature and the supernatant was removed. Spores were resuspended in 6 μl of fresh germination buffer. 2 μl of the reaction was placed onto a glass slide and sealed with a #1.5 18 x 18 mm coverslip. Spores were imaged using a Nikon Eclipse Ti microscope with a Nikon 60x N.A. 1.4 oil immersion Plan Apochromat Ph3 phase-contrast objective lens. A Zyla 5.5 megapixel sCMOS camera was used at 126 ms exposure time, and no binning was applied.

Live-cell imaging of nuclear transport. 4 μl of purified *A. algerae* spores obtained from *H. zea* ($6x10^7$ spores/ml) was mixed with 40 μl of NucBlue (Invitrogen, catalog #R37605) and incubated at 25˚C for 40 min. Spores were then centrifuged at 5,000 g for 1 min at room temperature and the supernatant was removed. 10 μl of germination buffer was added to the pre-stained spores and stored on ice prior to imaging. 2 μl of this reaction was added to a poly-L-

lysine coated glass slide and covered with a #1.5 18 x 18 mm coverslip. To test the effect of NucBlue on germination, we compared percent germination in the presence and absence of NucBlue for 3 batches of spores. The average percent germination is 51% in the control group (without NucBlue), while it is 40% when pre-incubated with NucBlue. The difference observed is not statistically significant (unpaired Student's t-test, p = 0.306; S12 Fig).

To image nuclear movement inside the spore coat prior to translocation into the PT, imaging was performed on a Nikon Eclipse Ti microscope with Nikon 60x N.A. 1.4 oil immersion Plan Apochromat Ph3 objective lens. Intensity of fluorescent excitation and intensity of transmitted light were balanced to allow simultaneous single channel single camera imaging (Duodetection). A Zyla 5.5 megapixel sCMOS camera was used, providing a wide field of view at 28 frames per second with 30 ms exposure time, no binning was applied.

To observe nuclear translocation through the PT, imaging was performed on a Zeiss AxioObserver Z1 with 40x N.A. 1.3 EC Plan-Neofluar oil immersion objective lens. An Axiocam 503 Monochrome CCD camera was used, yielding 20 frames per second with 45 ms exposure time, and 3x3 binning was applied.

Image analysis. Kymographs of the PT germination were generated from movies using Fiji software[82] with the straighten function. Measurement of the PT length was quantified from raw time-lapse images using Fiji software[82]. The PT was traced using the segmented line function. The maximum PT length was defined from the exit site from the spore body to the point where the infectious cargo connects to the PT. Velocity and acceleration of the PT firing process were calculated by $\Delta y/\Delta x$, where Δy is the change in PT length or the change in velocities, and Δx is the corresponding time interval. Graphs were plotted using GraphPad Prism 8 software. Fitting of data in Fig 4B was performed using a 'sigmoidal, 4PL, X is concentration' equation. R^2 values were 0.89 for *A. algerae*, 0.60 for *E. hellem*, and 0.93 for *E. intestinalis*.

For nuclear translocation, the kymographs were analyzed using Fiji software[82]. Speed of nuclear translocation was measured from changes of the distance of nuclear signals divided by the corresponding time interval. The aspect ratio of the nuclear deformation was quantified by the width (W) divided by the height (H) of nuclear signals from seven kymographs. The aspect ratio for the nucleus in the PT is measured during the pause phase of transport to minimize the impact of blurring due to movement, and the aspect ratio for the nucleus outside the tube is measured when it emerges at the distal end of the PT.

Validation of PT length comparison between pre-germination and post-germination states

Our measurements of PT length inside the spore (pre-germination) are made from analyzing SBFSEM data, while measurements of the PT outside the spore (post-germination) are made using optical microscopy. To assess whether measurements from these methods are comparable, we measured the spore length for *E. hellem* from both these techniques. The spore length obtained from SBFSEM and LM are similar (2.8 ± 0.3 μm). These results validate comparing measurements between the two methods.

Statistical analyses

GraphPad Prism 8 software was used for all statistical analyses. In all analyses, we used a two-tailed unpaired Student's t-test to compare the difference between two groups, with the exception of two analyses: 1) PT shortening after germination and 2) the nuclear aspect ratio. For PT shortening after germination, both a one sample t-test and a two-tailed paired Student's t-test were used. For the nuclear aspect ratio, a two-tailed paired Student's t-test was used. P values are reported in the figure legends.

Supporting information

S1 Fig. Quantification of volume and dimensions of spore organelles from SBFSEM. (a) Quantification of spore dimensions. **(b)** Quantification of volumes. Organelle volumes as a percentage of the entire spore volume are noted on the graph. **(c)** Number of PT coils quantified from 3D reconstruction of spores. **(d)** Quantification of the angle between PT coils and the A-P axis. All error bars in this figure represent standard deviation (n = 19 for *A. algerae* and n = 23 for *E. hellem*).
(TIF)

S2 Fig. Possible models of how the linear and coiled parts of the PT are connected. Schematic diagrams showing two possible models of the connection between straight and coiled regions of the PT. Red arrows indicate the region where the PT is straight. Model 1 was proposed by Cali *et al*[*46*].
(TIF)

S3 Fig. Representative SBFSEM slices through spores with tangled PT ends. Three representative SBFSEM sections originating from spores with tangled PT ends, as described in Fig 2D. Red arrows indicate the PT.
(TIF)

S4 Fig. 2D TEM images of *A. algerae* and *E. hellem* spores. TEM sections of **(a)** *A. algerae* spores and **(b)** *E. hellem* spore indicating structures inside the spore, including exospore (Ex), endospore (En), anchoring disc (AD), anterior polaroplast (AP), posterior polaroplast (PP), polar tube (PT), nucleus (N), and vacuole (V). These samples were used for SBFSEM experiments. The right panel of (a) is the same as that shown in Fig 2E, but without color overlay.
(TIF)

S5 Fig. *A. algerae* PT length as a function of time during the germination process. Graphs represent polar tube length over the time period of PT germination for 20 individual spores. See S2 Table for data used to generate these plots.
(TIF)

S6 Fig. *E. hellem* PT length as a function of time during the germination process. Graphs represent polar tube length over the time period of PT germination for 20 individual spores. See S2 Table for data used to generate these plots.
(TIF)

S7 Fig. *E. intestinalis* PT length as a function of time during the germination process. Graphs represent polar tube length over the time period of PT germination from 20 individual spores. See S2 Table for data used to generate these plots.
(TIF)

S8 Fig. Location of PT emergence from the spores. For *A. algerae*, 100% of the PTs emerge from the center (apical tip) of the spore, while for *E. hellem* and *E. intestinalis* 69% and 88% of PTs emerge off-center relative to the apical tip, respectively.
(TIF)

S9 Fig. Quantification of PT lengths at different stages, and time spent in phase II of the PT germination. (a) Graph showing the maximum length and the length of the PT at 3 sec after germination is complete, ****$p<0.0001$ (paired Student's t-test). **(b)** Same data as in (a). Each line connects the PT from the same spore, before and after shortening. **(c)** Time spent in phase II of germination, when the PT is static. **(d)** Quantification of PT length in the intact

spores from SBFSEM and the length of fully extended PT from optical microscopy. The graph is the same as presented in Fig 4H, but with individual data points plotted. ****p<0.0001 (unpaired Student's t-test). Error bars in this figure represent standard deviations (n = 20 for each species).
(TIF)

S10 Fig. Examples of incomplete germination events. (a) Kymographs of incomplete spore germination from *A. algerae*, *E. hellem*, and *E. intestinalis*. Scale bar for time is shown on the X-axis and for distance on the Y-axis. For incomplete germination events observed, the distal end of the tube appeared to be straight, in contrast to the hooked ends usually observed for complete germination[25]. **(b)** PT length quantified from incomplete germination events. **(C)** Quantification of the time for the PT to reach $\geq$ 90% of its maximum length. The error bars in this figure represent standard deviation (n = 3 for each species).
(TIF)

S11 Fig. Nuclei imaged during PT germination. (a) Additional time-lapse images of fluorescently labeled nuclei inside spores during PT germination. Top and bottom represent two individual spores. Time intervals are 50 ms. Black arrows indicate the frame in which the nuclei have begun to enter the PT. **(b)** Additional kymograph of the nuclear translocation through the PT. **(c)** Quantification of the nuclear position relative to spore coat over time (n = 4). **(d)** Graph showing maximum velocity of the cargo transport process. The data was calculated from (c). Error bar represents standard deviation (n = 4). A total of seven movies were recorded to monitor nuclear transport. However, the nuclear signal in the first few frames of the movie was below our detection threshold for three of these movies, which have not been quantified here.
(TIF)

S12 Fig. NucBlue does not impact *A. algerae* spore germination. Graph indicates percent germination of spores in the presence or absence of NucBlue (3 independent preparations of *A. algerae* spores; ns = not statistically significant; p = 0.306, unpaired Student's t-test).
(TIF)

S1 Table. Measurements obtained from SBFSEM experiments.
(XLSX)

S2 Table. Length Vs. time measurements from live-cell imaging of PT germination.
(XLSX)

S1 Video. 3D reconstruction of A. *algerae* spore from SBFSEM. Representative 3D reconstruction of an *A. algerae* spore. At the beginning of the video, slices through the spore are shown. Each color represents an individual organelle: exospore (orange), endospore (yellow), PT (blue), vacuole (red), posterior polaroplast (purple), and anchoring disc (green).
(MOV)

S2 Video. 3D reconstruction of *E. hellem* spore from SBFSEM. Representative 3D reconstruction of an *E. hellem* spore. Each color represents an individual organelle: exospore (orange), endospore (yellow), PT (blue), anterior polaroplast (pink), and anchoring disc (green).
(MOV)

S3 Video. Live-cell imaging of *A. algerae* PT germination. Time-lapse video of PT germination in *A. algerae*, corresponding to Fig 4A.
(MOV)

S4 Video. Live-cell imaging of *E. hellem* PT germination. Time-lapse video of PT germination in *E. hellem*, corresponding to Fig 4A.
(MOV)

S5 Video. Live-cell imaging of *E. intestinalis* PT germination. Time-lapse video of PT germination in *E. intestinalis*, corresponding to Fig 4A.
(MOV)

S6 Video. Live-cell imaging of *E. hellem* PT shortening after germination. Time-lapse video of the PT germination in *E. hellem*, corresponding to Fig 4F. After the emergence of the infectious cargo at the end of the PT, the PT starts to shrink. However, rather than a synchronized shortening of the entire tube across its complete length, segments of the tube appear to contract at slightly different times.
(MOV)

S7 Video. Incomplete germination event for *A. algerae*. Time-lapse video of incomplete PT germination in *A. algerae*.
(MOV)

S8 Video. Incomplete germination event for *E. hellem*. Time-lapse video of incomplete PT germination in *E. hellem*.
(MOV)

S9 Video. Incomplete germination for *E. intestinalis*. Time-lapse video of incomplete PT germination in *E. intestinalis*.
(MOV)

S10 Video. Nucleus movement inside the spore prior to translocation through the PT. Time-lapse images of *A. algerae* nucleus inside the spore. Dual detection of NucBlue fluorescence and transmitted light was applied in order to visualize both the DNA and PT simultaneously.
(MOV)

S11 Video. Nucleus movement through the PT. Time-lapse video of *A. algerae* nuclear transport through the PT.
(MOV)

Acknowledgments

Author Contributions

Conceptualization: Pattana Jaroenlak, Feng-Xia Liang, Damian C. Ekiert, Gira Bhabha.

Formal analysis: Pattana Jaroenlak, Alina Davydov, Mahrukh Usmani, Damian C. Ekiert, Gira Bhabha.

References

1. Frénal K, Dubremetz J-F, Lebrun M, Soldati-Favre D. Gliding motility powers invasion and egress in Apicomplexa. Nat Rev Microbiol. 2017; 15: 645–660. https://doi.org/10.1038/nrmicro.2017.86 PMID: 28867819

2. Pillich H, Puri M, Chakraborty T. ActA of Listeria monocytogenes and Its Manifold Activities as an Important Listerial Virulence Factor. Curr Top Microbiol Immunol. 2017; 399: 113–132. https://doi.org/10.1007/82_2016_30 PMID: 27726006

3. Epting CL, Coates BM, Engman DM. Molecular mechanisms of host cell invasion by Trypanosoma cruzi. Exp Parasitol. 2010; 126: 283–291. https://doi.org/10.1016/j.exppara.2010.06.023 PMID: 20599990

4. Keeling PJ, Doolittle WF. Alpha-tubulin from early-diverging eukaryotic lineages and the evolution of the tubulin family. Mol Biol Evol. 1996; 13: 1297–1305. https://doi.org/10.1093/oxfordjournals.molbev.a025576 PMID: 8952074

5. Lee SC, Corradi N, Byrnes EJ, Torres-Martinez S, Dietrich FS, Keeling PJ, et al. Microsporidia Evolved from Ancestral Sexual Fungi. Current Biology. 2008. pp. 1675–1679. https://doi.org/10.1016/j.cub.2008.09.030 PMID: 18976912

6. Troemel ER, Félix M-A, Whiteman NK, Barrière A, Ausubel FM. Microsporidia are natural intracellular parasites of the nematode Caenorhabditis elegans. PLoS Biol. 2008; 6: 2736–2752. https://doi.org/10.1371/journal.pbio.0060309 PMID: 19071962

7. Zhang G, Sachse M, Prevost M-C, Luallen RJ, Troemel ER, Félix M-A. A Large Collection of Novel Nematode-Infecting Microsporidia and Their Diverse Interactions with Caenorhabditis elegans and Other Related Nematodes. PLoS Pathog. 2016; 12: e1006093. https://doi.org/10.1371/journal.ppat.1006093 PMID: 27942022

8. Fries I, Martín R, Meana A, García-Palencia P, Higes M. Natural infections of Nosema ceranae in European honey bees. Journal of Apicultural Research. 2006. pp. 230–233. https://doi.org/10.3896/ibra.1.45.4.13

9. Becnel JJ, Sprague V, Fukuda T, Hazard EI. Development ofEdhazardia aedis(Kudo, 1930) N. G., N. Comb. (Microsporida: Amblyosporidae) in the MosquitoAedes aegypti(L.) (Diptera: Culicidae). The Journal of Protozoology. 1989. pp. 119–130. https://doi.org/10.1111/j.1550-7408.1989.tb01057.x PMID: 2724178

10. Palenzuela O, Redondo MJ, Cali A, Takvorian PM, Alonso-Naveiro M, Alvarez-Pellitero P, et al. A new intranuclear microsporidium, Enterospora nucleophila n. sp., causing an emaciative syndrome in a piscine host (Sparus aurata), prompts the redescription of the family Enterocytozoonidae. International Journal for Parasitology. 2014. pp. 189–203. https://doi.org/10.1016/j.ijpara.2013.10.005 PMID: 24326177

11. Scurrell E, Manning S, Malho P, Civello A, Mould J, Carrozza R, et al. Microsporidial keratopathy in two dogs. Veterinary Ophthalmology. 2019. https://doi.org/10.1111/vop.12726 PMID: 31758652

12. Croppo GP, Croppo GP, Moura H, Da Silva AJ, Leitch GJ, Moss DM, et al. Ultrastructure, immunofluorescence, western blot, and PCR analysis of eight isolates of Encephalitozoon (Septata) intestinalis established in culture from sputum and urine samples and duodenal aspirates of five patients with AIDS. J Clin Microbiol. 1998; 36: 1201–1208. https://doi.org/10.1128/JCM.36.5.1201-1208.1998 PMID: 9574677

13. Cali A, Kotler DP, Orenstein JM. Septata Intestinalis N. G., N. Sp., an Intestinal Microsporidian Associated With Chronic Diarrhea and Dissemination In Aids Patients. The Journal of Eukaryotic Microbiology. 1993. pp. 101–112. https://doi.org/10.1111/j.1550-7408.1993.tb04889.x PMID: 8457797

14. Friedberg DN, Stenson SM, Orenstein JM, Tierno PM, Charles NC. Microsporidial keratoconjunctivitis in acquired immunodeficiency syndrome. Arch Ophthalmol. 1990; 108: 504–508. https://doi.org/10.1001/archopht.1990.01070060052047 PMID: 2108656

15. Teachey DT, Russo P, Orenstein JM, Didier ES, Bowers C, Bunin N. Pulmonary infection with microsporidia after allogeneic bone marrow transplantation. Bone Marrow Transplant. 2004; 33: 299–302. https://doi.org/10.1038/sj.bmt.1704327 PMID: 14628080

16. Yachnis AT, Berg J, Martinez-Salazar A, Bender BS, Diaz L, Rojiani AM, et al. Disseminated microsporidiosis especially infecting the brain, heart, and kidneys. Report of a newly recognized pansporoblastic species in two symptomatic AIDS patients. Am J Clin Pathol. 1996; 106: 535–543. https://doi.org/10.1093/ajcp/106.4.535 PMID: 8853044

17. Katinka MD, Duprat S, Cornillot E, Méténier G, Thomarat F, Prensier G, et al. Genome sequence and gene compaction of the eukaryote parasite Encephalitozoon cuniculi. Nature. 2001; 414: 450–453. https://doi.org/10.1038/35106579 PMID: 11719806

18. Dean P, Sendra KM, Williams TA, Watson AK, Major P, Nakjang S, et al. Transporter gene acquisition and innovation in the evolution of Microsporidia intracellular parasites. Nat Commun. 2018; 9: 1709. https://doi.org/10.1038/s41467-018-03923-4 PMID: 29703975

19. Han B, Takvorian PM, Weiss LM. Invasion of Host Cells by Microsporidia. Front Microbiol. 2020; 11: 172. https://doi.org/10.3389/fmicb.2020.00172 PMID: 32132983

20. Kudo R. Experiments on the Extrusion of Polar Filaments of Cnidosporidian Spores. The Journal of Parasitology. 1918. p. 141. https://doi.org/10.2307/3271239

21. Lom J. On the structure of the extruded microsporidian polar filament. Zeitschrift für Parasitenkunde. 1972. pp. 200–213. https://doi.org/10.1007/bf00329598

22. Weidner E. Ultrastructural study of microsporidian invasion into cells. Z Parasitenkd. 1972; 40: 227–242. https://doi.org/10.1007/BF00329623 PMID: 4346238

23. Takvorian PM, Weiss LM, Cali A. The early events of Brachiola algerae (Microsporidia) infection: spore germination, sporoplasm structure, and development within host cells. Folia Parasitol. 2005; 52: 118–129. https://doi.org/10.14411/fp.2005.015 PMID: 16004371

24. Frixione E, Ruiz L, Santillán M, de Vargas LV, Tejero JM, Undeen AH. Dynamics of polar filament discharge and sporoplasm expulsion by microsporidian spores. Cell Motility and the Cytoskeleton. 1992. pp. 38–50. https://doi.org/10.1002/cm.970210105 PMID: 1531784

25. Takvorian PM, Han B, Cali A, Rice WJ, Gunther L, Macaluso F, et al. An Ultrastructural Study of the Extruded Polar Tube of Anncaliia algerae (Microsporidia). J Eukaryot Microbiol. 2020; 67: 28–44. https://doi.org/10.1111/jeu.12751 PMID: 31332877

26. Franzen C, Müller A, Hartmann P, Salzberger B. Cell invasion and intracellular fate of Encephalitozoon cuniculi (Microsporidia). Parasitology. 2005; 130: 285–292. https://doi.org/10.1017/s003118200400633x PMID: 15796011

27. Wittner M, Weiss LM. The Microsporidia and Microsporidiosis. Amer Society for Microbiology; 1999.

28. Weidner E. The microsporidian spore invasion tube. The ultrastructure, isolation, and characterization of the protein comprising the tube. The Journal of Cell Biology. 1976. pp. 23–34. https://doi.org/10.1083/jcb.71.1.23 PMID: 10309

29. Bigliardi E, Riparbelli MG, Selmi MG, Lanzarini P, Corona S, Gatti S, et al. Mechanisms of Microsporidial Cell Division: Ultrastructural Study on Encephalitozoon hellem. The Journal of Eukaryotic Microbiology. 1998. pp. 347–351. https://doi.org/10.1111/j.1550-7408.1998.tb04547.x PMID: 9627995

30. Bigliardi E, Sacchi L. Cell biology and invasion of the microsporidia. Microbes Infect. 2001; 3: 373–379. https://doi.org/10.1016/s1286-4579(01)01393-4 PMID: 11369274

31. Gavelis GS, Wakeman KC, Tillmann U, Ripken C, Mitarai S, Herranz M, et al. Microbial arms race: Ballistic "nematocysts" in dinoflagellates represent a new extreme in organelle complexity. Science Advances. 2017. p. e1602552. https://doi.org/10.1126/sciadv.1602552 PMID: 28435864

32. Nüchter T, Benoit M, Engel U, Ozbek S, Holstein TW. Nanosecond-scale kinetics of nematocyst discharge. Curr Biol. 2006; 16: R316–8. https://doi.org/10.1016/j.cub.2006.03.089 PMID: 16682335

33. Cali A, Weiss LM, Takvorian PM. Brachiola algerae Spore Membrane Systems, their Activity During Extrusion, and a New Structural Entity, the Multilayered Interlaced Network, Associated with the Polar Tube and the Sporoplasm. The Journal of Eukaryotic Microbiology. 2002. pp. 164–174. https://doi.org/10.1111/j.1550-7408.2002.tb00361.x PMID: 12043963

34. Troemel ER, Becnel JJ. Genome analysis and polar tube firing dynamics of mosquito-infecting microsporidia. Fungal Genet Biol. 2015; 83: 41–44. https://doi.org/10.1016/j.fgb.2015.08.007 PMID: 26300319

35. Franzen C, Fischer S, Schroeder J, Schölmerich J, Schneuwly S. Morphological and molecular investigations of Tubulinosema ratisbonensis gen. nov., sp. nov. (Microsporidia: Tubulinosematidae fam.

nov.), a parasite infecting a laboratory colony of Drosophila melanogaster (Diptera: Drosophilidae). J Eukaryot Microbiol. 2005; 52: 141–152. https://doi.org/10.1111/j.1550-7408.2005.04-3324.x PMID: 15817119

36. Tourtip S, Wongtripop S, Stentiford GD, Bateman KS, Sriurairatana S, Chavadej J, et al. Enterocytozoon hepatopenaei sp. nov. (Microsporida: Enterocytozoonidae), a parasite of the black tiger shrimp Penaeus monodon (Decapoda: Penaeidae): Fine structure and phylogenetic relationships. J Invertebr Pathol. 2009; 102: 21–29. https://doi.org/10.1016/j.jip.2009.06.004 PMID: 19527727

37. Denk W, Horstmann H. Serial block-face scanning electron microscopy to reconstruct three-dimensional tissue nanostructure. PLoS Biol. 2004; 2: e329. https://doi.org/10.1371/journal.pbio.0020329 PMID: 15514700

38. Vavra J, Undeen AH. Nosema algeraen. sp. (Cnidospora, Microsporida) a Pathogen in a Laboratory Colony ofAnopheles stephensiListon (Diptera, Culicidae). The Journal of Protozoology. 1970. pp. 240–249. https://doi.org/10.1111/j.1550-7408.1970.tb02365.x PMID: 4915459

39. Sutrave G, Maundrell A, Keighley C, Jennings Z, Brammah S, Wang M-X, et al. Anncaliia algerae Microsporidial Myositis, New South Wales, Australia. Emerg Infect Dis. 2018; 24: 1528–1531. https://doi.org/10.3201/eid2408.172002 PMID: 30014835

40. Cali A, Weiss LM, Takvorian PM. An analysis of the microsporidian genus Brachiola, with comparisons of human and insect isolates of Brachiola algerae. J Eukaryot Microbiol. 2004; 51: 678–685. https://doi.org/10.1111/j.1550-7408.2004.tb00608.x PMID: 15666726

41. Sokolova YY, Weidner E, DiMario PJ. Development of Anncaliia algerae (Microsporidia) in Drosophila melanogaster. J Eukaryot Microbiol. 2020; 67: 125–131. https://doi.org/10.1111/jeu.12762 PMID: 31529563

42. Smith D, Starborg T. Serial block face scanning electron microscopy in cell biology: Applications and technology. Tissue Cell. 2019; 57: 111–122. https://doi.org/10.1016/j.tice.2018.08.011 PMID: 30220487

43. Bigliardi E, Selmi MG, Lupetti P, Corona S, Gatti S, Scaglia M, et al. Microsporidian spore wall: ultrastructural findings on Encephalitozoon hellem exospore. J Eukaryot Microbiol. 1996; 43: 181–186. https://doi.org/10.1111/j.1550-7408.1996.tb01388.x PMID: 8640188

44. Franzen C. Microsporidia: how can they invade other cells? Trends Parasitol. 2004; 20: 275–279. https://doi.org/10.1016/j.pt.2004.04.009 PMID: 15147678

45. Chioralia G, Trammer T, Maier WA, Seitz HM. Morphologic changes in Nosema algerae (Microspora) during extrusion. Parasitol Res. 1998; 84: 123–131. https://doi.org/10.1007/s004360050368 PMID: 9493211

46. Cali A, Owen RL. Microsporidiosis. Laboratory Diagnosis of Infectious Diseases. Springer, New York, NY; 1988. pp. 929–950. https://doi.org/10.1007/978-1-4612-3898-0_98

47. Polonais V, Prensier G, Méténier G, Vivarès CP, Delbac F. Microsporidian polar tube proteins: highly divergent but closely linked genes encode PTP1 and PTP2 in members of the evolutionarily distant Antonospora and Encephalitozoon groups. Fungal Genet Biol. 2005; 42: 791–803. https://doi.org/10.1016/j.fgb.2005.05.005 PMID: 16051504

48. Bouzahzah B, Nagajyothi F, Ghosh K, Takvorian PM, Cali A, Tanowitz HB, et al. Interactions of Encephalitozoon cuniculi polar tube proteins. Infect Immun. 2010; 78: 2745–2753. https://doi.org/10.1128/IAI.01205-09 PMID: 20308291

49. Han B, Polonais V, Sugi T, Yakubu R, Takvorian PM, Cali A, et al. The role of microsporidian polar tube protein 4 (PTP4) in host cell infection. PLoS Pathog. 2017; 13: e1006341. https://doi.org/10.1371/journal.ppat.1006341 PMID: 28426751

50. Sokolova Y, Pelin A, Hawke J, Corradi N. Morphology and phylogeny of Agmasoma penaei (Microsporidia) from the type host, Litopenaeus setiferus, and the type locality, Louisiana, USA. Int J Parasitol. 2015; 45: 1–16. https://doi.org/10.1016/j.ijpara.2014.07.013 PMID: 25449947

51. Sokolova YY, Sakaguchi K, Paulsen DB. Establishing a New Species Encephalitozoon pogonae for the Microsporidian Parasite of Inland Bearded Dragon Pogona vitticeps Ahl 1927 (Reptilia, Squamata, Agamidae). J Eukaryot Microbiol. 2016; 63: 524–535. https://doi.org/10.1111/jeu.12296 PMID: 26785360

52. Weidner E, Byrd W, Scarborough A, Pleshinger J, Sibley D. Microsporidian Spore Discharge and the Transfer of Polaroplast Organelle Membrane into Plasma Membrane. The Journal of Protozoology. 1984. pp. 195–198. https://doi.org/10.1111/j.1550-7408.1984.tb02948.x

53. Kucerova Z, Moura H, Visvesvara GS, Leitch GJ. Differences between Brachiola (Nosema) algerae Isolates of Human and Insect Origin when Tested Using an In Vitro Spore Germination Assay anda Cultured Cell Infection Assay. The Journal of Eukaryotic Microbiology. 2004. pp. 339–343. https://doi.org/10.1111/j.1550-7408.2004.tb00577.x PMID: 15218704

54. Leitch GJ, He Q, Wallace S, Visvesvara GS. Inhibition of the spore polar filament extrusion of the microsporidium, Encephalitozoon hellem, isolated from an AIDS patient. J Eukaryot Microbiol. 1993; 40: 711–717. https://doi.org/10.1111/j.1550-7408.1993.tb04463.x PMID: 8292991

55. Aldama-Cano DJ, Sanguanrut P, Munkongwongsiri N, Ibarra-Gámez JC, Itsathitphaisarn O, Vanichviriyakit R, et al. Bioassay for spore polar tube extrusion of shrimp Enterocytozoon hepatopenaei (EHP). Aquaculture. 2018. pp. 156–161. https://doi.org/10.1016/j.aquaculture.2018.02.039

56. Liu H, Chen B, Hu S, Liang X, Lu X, Shao Y. Quantitative Proteomic Analysis of Germination of Nosema bombycis Spores under Extremely Alkaline Conditions. Frontiers in Microbiology. 2016. https://doi.org/10.3389/fmicb.2016.01459 PMID: 27708628

57. Vale RD, Coppin CM, Malik F, Kull FJ, Milligan RA. Tubulin GTP hydrolysis influences the structure, mechanical properties, and kinesin-driven transport of microtubules. J Biol Chem. 1994; 269: 23769–23775. PMID: 7916345

58. Toba S, Watanabe TM, Yamaguchi-Okimoto L, Toyoshima YY, Higuchi H. Overlapping hand-over-hand mechanism of single molecular motility of cytoplasmic dynein. Proceedings of the National Academy of Sciences. 2006. pp. 5741–5745. https://doi.org/10.1073/pnas.0508511103 PMID: 16585530

59. Håkansson S, Morisaki H, Heuser J, Sibley LD. Time-lapse video microscopy of gliding motility in Toxoplasma gondii reveals a novel, biphasic mechanism of cell locomotion. Mol Biol Cell. 1999; 10: 3539–3547. https://doi.org/10.1091/mbc.10.11.3539 PMID: 10564254

60. Deacon JW, Saxena G. Orientated zoospore attachment and cyst germination in Catenaria anguillulae, a facultative endoparasite of nematodes. Mycological Research. 1997. pp. 513–522. https://doi.org/10.1017/s0953756296003085

61. Weidner E, Manale SB, Halonen SK, Lynn JW. Protein-Membrane Interaction Is Essential to Normal Assembly of the Microsporidian Spore Invasion Tube. Biol Bull. 1995; 188: 128–135. https://doi.org/10.2307/1542078 PMID: 29281361

62. Undeen AH, Frixione E. The role of osmotic pressure in the germination of Nosema algerae spores. J Protozool. 1990; 37: 561–567. https://doi.org/10.1111/j.1550-7408.1990.tb01265.x PMID: 2086785

63. Keohane EM, Weiss LM. Characterization and function of the microsporidian polar tube: a review. Folia Parasitol. 1998; 45: 117–127. PMID: 9684322

64. Weidner E. The microsporidian spore invasion tube. III. Tube extrusion and assembly. The Journal of Cell Biology. 1982. pp. 976–979. https://doi.org/10.1083/jcb.93.3.976 PMID: 7119008

65. Liu T-L, Upadhyayula S, Milkie DE, Singh V, Wang K, Swinburne IA, et al. Observing the cell in its native state: Imaging subcellular dynamics in multicellular organisms. Science. 2018; 360. https://doi.org/10.1126/science.aaq1392 PMID: 29674564

66. de Oliveira S, Rosowski EE, Huttenlocher A. Neutrophil migration in infection and wound repair: going forward in reverse. Nat Rev Immunol. 2016; 16: 378–391. https://doi.org/10.1038/nri.2016.49 PMID: 27231052

67. Reymond N, d'Água BB, Ridley AJ. Crossing the endothelial barrier during metastasis. Nat Rev Cancer. 2013; 13: 858–870. https://doi.org/10.1038/nrc3628 PMID: 24263189

68. Denais CM, Gilbert RM, Isermann P, McGregor AL, te Lindert M, Weigelin B, et al. Nuclear envelope rupture and repair during cancer cell migration. Science. 2016; 352: 353–358. https://doi.org/10.1126/science.aad7297 PMID: 27013428

69. Raab M, Gentili M, de Belly H, -R. Thiam H, Vargas P, Jimenez AJ, et al. ESCRT III repairs nuclear envelope ruptures during cell migration to limit DNA damage and cell death. Science. 2016. pp. 359–362. https://doi.org/10.1126/science.aad7611 PMID: 27013426

70. Matsumoto A, Hieda M, Yokoyama Y, Nishioka Y, Yoshidome K, Tsujimoto M, et al. Global loss of a nuclear lamina component, lamin A/C, and LINC complex components SUN1, SUN2, and nesprin-2 in breast cancer. Cancer Med. 2015; 4: 1547–1557. https://doi.org/10.1002/cam4.495 PMID: 26175118

71. Venables RS, McLean S, Luny D, Moteleb E, Morley S, Quinlan RA, et al. Expression of individual lamins in basal cell carcinomas of the skin. Br J Cancer. 2001; 84: 512–519. https://doi.org/10.1054/bjoc.2000.1632 PMID: 11207047

72. Broers JL, Raymond Y, Rot MK, Kuijpers H, Wagenaar SS, Ramaekers FC. Nuclear A-type lamins are differentially expressed in human lung cancer subtypes. Am J Pathol. 1993; 143: 211–220. PMID: 8391215

73. Wu Z, Wu L, Weng D, Xu D, Geng J, Zhao F. Reduced expression of lamin A/C correlates with poor histological differentiation and prognosis in primary gastric carcinoma. J Exp Clin Cancer Res. 2009; 28: 8. https://doi.org/10.1186/1756-9966-28-8 PMID: 19144202

74. Harada T, Swift J, Irianto J, Shin J-W, Spinler KR, Athirasala A, et al. Nuclear lamin stiffness is a barrier to 3D migration, but softness can limit survival. J Cell Biol. 2014; 204: 669–682. https://doi.org/10.1083/jcb.201308029 PMID: 24567359

75. Rowat AC, Jaalouk DE, Zwerger M, Ung WL, Eydelnant IA, Olins DE, et al. Nuclear envelope composition determines the ability of neutrophil-type cells to passage through micron-scale constrictions. J Biol Chem. 2013; 288: 8610–8618. https://doi.org/10.1074/jbc.M112.441535 PMID: 23355469

76. Melcer S, Gruenbaum Y, Krohne G. Invertebrate lamins. Experimental Cell Research. 2007. pp. 2157–2166. https://doi.org/10.1016/j.yexcr.2007.03.004 PMID: 17451683

77. Dittmer TA, Misteli T. The lamin protein family. Genome Biology. 2011. p. 222. https://doi.org/10.1186/gb-2011-12-5-222 PMID: 21639948

78. Aurrecoechea C, Barreto A, Brestelli J, Brunk BP, Caler EV, Fischer S, et al. AmoebaDB and MicrosporidiaDB: functional genomic resources for Amoebozoa and Microsporidia species. Nucleic Acids Res. 2011; 39: D612–9. https://doi.org/10.1093/nar/gkq1006 PMID: 20974635

79. Corradi N, Pombert J-F, Farinelli L, Didier ES, Keeling PJ. The complete sequence of the smallest known nuclear genome from the microsporidian Encephalitozoon intestinalis. Nat Commun. 2010; 1: 77. https://doi.org/10.1038/ncomms1082 PMID: 20865802

80. Solter LF, Becnel JJ, Vávra J. Research methods for entomopathogenic microsporidia and other protists. Manual of Techniques in Invertebrate Pathology. 2012. pp. 329–371. https://doi.org/10.1016/b978-0-12-386899-2.00011–7

81. Weiss LM, Delbac F, Russell Hayman J, Pan G, Dang X, Zhou Z. The Microsporidian Polar Tube and Spore Wall. Microsporidia. 2014. pp. 261–306. https://doi.org/10.1002/9781118395264.ch10

82. Schindelin J, Arganda-Carreras I, Frise E, Kaynig V, Longair M, Pietzsch T, et al. Fiji: an open-source platform for biological-image analysis. Nat Methods. 2012; 9: 676–682. https://doi.org/10.1038/nmeth.2019 PMID: 22743772

83. Pettersen EF, Goddard TD, Huang CC, Couch GS, Greenblatt DM, Meng EC, et al. UCSF Chimera—a visualization system for exploratory research and analysis. J Comput Chem. 2004; 25: 1605–1612. https://doi.org/10.1002/jcc.20084 PMID: 15264254